



Wave-ice interaction strengthens eddy activity in Fram Strait

Yi Liu^{1,3}, Yunhan Yang¹, Haijin Dai^{1,2*}, Jun Zhao^{1*}, Qiang Li³

¹College of Meteorology and Oceanography, National University of Defense Technology, Changsha, 410073, China

²Key Laboratory of High Impact Weather (special), China Meteorological Administration, Changsha, 410073, China

5 ³College of Ocean and Meteorology, Guangdong Ocean University, Zhanjiang, 52488, China

Correspondence to: Haijin Dai (hj_dai@nudt.edu.cn) and Jun Zhao (zhaojun@nudt.edu.cn)

Abstract. A mesoscale eddy was detected by satellite in the MIZ of Fram Strait and verified by reference to the barotropic instability of the East Greenland Current (EGC). According to the reanalysis data, the eddy originated from a mother eddy that grew and diminished in a branch of EGC during the summer. After September 12, this branch of the EGC strengthened and became equally strong as the main body of the EGC by the end of September. As a result, the eddy grew into a strong mesoscale eddy, which was captured on October 4 by satellite. The strengthening of the branch may be attributed to the influence of wave-ice interactions. In September, sea ice expanded toward the open ocean as a result of the seasonal cycle and covered the branch of the EGC. Wave-ice interactions and eddy genesis were revealed by numerical simulations. When waves propagated into the ice zone, they dissipated quickly at the ice edge and produce an ice-edge jet, thus strengthening the background flow. The resulting enhanced barotropic instability helped small turbulence grow into large eddies. During the same period, an ocean front grew due to ice formation and dense water sinking, thus indicating that baroclinic instability may not play an important role in eddy genesis.

1 Introduction

The Fram Strait [64°N-82°N, 30°W-20°E], which represents the only channel for deep water exchange between the Arctic and other regions, is located between Greenland and the Svalbard Archipelago. On the western side, the East Greenland Current (EGC) originates from Fram Strait and moves equatorward until it reaches Cape Farewell at a speed of 0.3-0.5 cm/s. On the eastern side, the Norwegian Atlantic Slope Current (NwASC) and Norwegian Atlantic Front Current (NwAFC) move poleward anticyclonically and cyclonically, respectively. The NwASC and the NwAFC merge into the West Spitsbergen Current before passing through Fram Strait and the inflow from the Atlantic Ocean. EGC moves equatorward in the whole layer, which transports Arctic outflow in both the surface layer and the deep layer (Aksenov et al. 2016). Previous studies (Sutherland and Pickart, 2008; Haine et al. 2015; Aksenov et al. 2016) have indicated that the EGC is driven not only by dense overflows from the Arctic but also by wind forcing and constrained by the local topography. An issue rises that (1) Are there other significant mechanisms that contribute to the EGC? In addition, ocean eddies detected in or close to the EGC constitute a notable phenomenon.



30 Ocean eddies, which feature typical horizontal scales of 5–100 km, exhibit fast-moving (i.e., 0.7 m/s) circular currents. Previous studies (McWilliams 2016, Torres et al. 2018) defined ocean motions with horizontal scales of 50–300 km and 1–50 km as mesoscale motions and submesoscale motions, respectively. Ocean eddies are also called mesoscale eddies (Zhang et al 2016) or submesoscale eddies. Ocean eddies are typically larger at mid–low latitudes than at high latitudes due to the reduced Rossby radius (Manley and Hunkins 1985), which leads to submesoscale eddies appearing more frequently at high latitudes (Iakovlev 2018). According to both in situ observations (Zhao et al 2014) and numerical simulations (Li et al 2024), most Arctic eddies occur in the Chukchi–Beaufort Sea, Fram Strait and Barents-Kara Sea.

The marginal ice zone (MIZ), which is the transition zone between the open ocean and the ice-covered zone (Dumont et al 2011), is important for the occurrence of Arctic eddies, since it experiences numerous processes of atmosphere-ocean-ice-wave interactions, such as the heat exchange among air, sea and ice leading to ice formation or melt (Josberger 1983, Toyota et al 2016), the ocean–ice interfacial stress leading to current convergence/divergence, and salt rejection leading to deep water formation (Ivanov and Shapiro 2005) and wave energy dissipation (Wadhams and Holt 1991, Squire et al 1995, Squire 2007, Dai et al 2019). After 3 years of continuous observations (marginal ice zone experiment, MIZEX group, 1986), Johannnesen et al. (1987) proposed four mechanisms for eddy generation in the MIZ: (1) The variation in water depth leads to eddies via potential vorticity conservation, which is called a topographic controlled mechanism (Häkkinen 1987, Gula et al 2016); (2) The nonuniform current increases the vorticity via convergence, which is called the nonlinear advection mechanism (Häkkinen 1986, Dai et al 2017); (3) Horizontal velocity shear, which occurs between the jet and surrounding flow, produces eddies via the barotropic instability mechanism (Liu et al 1993, Dai et al 2019); and (4) Ocean fronts slump and produce eddies via a baroclinic instability mechanism. Specifically, the front can be produced by sea-ice melt (Manucharyan et al 2017) or dense water transport (Paquette and Bourke 1981, Zhang et al 2019). Among them, Dai et al. (2019) proposed a mechanism of barotropic instability whereby wave-ice interactions generate along-ice-edge jets and mesoscale eddies. Unfortunately, observational evidence to support this mechanism remains scarce. This raises two critical questions: (2) Can the entire process be observed in the real world? (3) What are the limiting factors for the occurrence of this mechanism? To solve the three issues above, this paper is organized as follows: Section 2 introduces the data and methods used in this study, Section 3 describes the eddy genesis process, and Section 4 provides a summary and identifies topics for future research.

Usually, in situ photography and/or satellite detection can be used to identify surface eddies since sea ice moves following (anti)cyclonic flows. However, eddies covered by frozen ice or occurring in the subsurface (Hunkins 1974, Dai et al. 2025) can be detected only by mooring. In this study, we investigate a surface eddy detected in the Fram Strait, where the topography is relatively flat and the water depth is greater than 250 m. The topographic controlled mechanism and nonlinear advection mechanism are excluded in this study.



2 Observational data and numerical experiments

2.1 Satellite image and reanalysis data

Satellite data are acquired from the European Remote Sensing Satellite (ERS-1), which was launched by the European Space Agency (ESA) on July 17, 1991. Synthetic Aperture Radar (SAR) images (<https://search.asf.alaska.edu/#/>) that feature a
65 spatial resolution of 25 m and color contrast between ice and water are utilized to identify mesoscale eddies within the marginal ice zone (MIZ) of the Fram Strait (Bashmachnikov et al. 2020). Numerous eddies have been captured in these SAR images in recent decades. A characteristic eddy (Fig. 1a), detected at 77.2° – 77.7° N, 7° – 9° W and observed from July 1 to October 4, 2020, is selected to illustrate eddy genesis in the Fram Strait. Topographic forcing and nonlinear advection mechanisms have been excluded as primary drivers in the preceding section. Barotropic instability and baroclinic instability
70 are examined for eddy evolution.

To investigate the mechanism underlying the genesis of the submesoscale eddy detected by SAR imagery and characterize its evolving environmental context, oceanic reanalysis data are employed to demonstrate how the eddy and the corresponding environment evolved. Daily oceanic reanalysis data obtained from the Mercator Center include temperature, current, salinity, and sea ice data with a horizontal resolution of $1/12^{\circ}$ and are used to demonstrate eddy evolution. This
75 dataset is generated by a global ocean eddy-resolving model (Copernicus Marine Environment Monitoring Service, CMEMS), which is driven by atmospheric forcing (ERA-Interim and ERA5) and assimilates observations via a reduced-order Kalman filter. Wave reanalysis data are derived from a wave spectrum model (Météo-France wave model, MFWAM), with a horizontal resolution of $1/5^{\circ}$. These data are used to demonstrate the evolution of the eddy and its corresponding environment. Hourly atmospheric reanalysis data obtained from the ECWMF (Hersbach et al. 2023) include surface wind
80 information.

2.2 Numerical experiments

In this study, we employed a coupled modeling framework to investigate eddy genesis. This framework integrates a sea ice model (Simple Sea Ice Model, SSIM; Dai et al. 2019), a wave model (Uchiyama et al. 2010), and an ocean model (Regional Ocean Modeling System, ROMS; Shchepetkin and McWilliams 2005). Following McWilliams et al. (2004), Shchepetkin
85 and McWilliams (2005), Uchiyama et al. (2010) and Dai et al. (2019), the governing equations in the coupled ocean-ice-wave model (ROMS-SSIM) are writing as:

Ocean model:

$$\frac{\partial \mathbf{u}}{\partial t} + \mathbf{u} \nabla_{\perp} \mathbf{u} + w \frac{\partial \mathbf{u}}{\partial z} = -\nabla_{\perp}(\phi + H) - f \hat{\mathbf{z}} \times \mathbf{u} + \gamma \nabla^2 \mathbf{u} + (1 - a_i) \boldsymbol{\tau}_{aw} + a_i \boldsymbol{\tau}_{wi} + \mathbf{J} + \mathbf{F}^w \quad , (1)$$

$$\frac{\partial \phi}{\partial z} + \frac{g\rho}{\rho_0} = -\frac{\partial \mathcal{H}}{\partial z} + K \quad , (2)$$



$$90 \quad \nabla_{\perp} \mathbf{u} + \frac{\partial \mathbf{w}}{\partial z} = 0 \quad , (3)$$

$$\frac{\partial c}{\partial t} + \mathbf{u} \nabla_{\perp} c + w \frac{\partial c}{\partial z} - \kappa = -(\mathbf{u}^{st} \cdot \nabla_{\perp})c - w^{st} \frac{\partial c}{\partial z} + \frac{1}{2} \frac{\partial}{\partial z} \left[\mathcal{E} \frac{\partial c}{\partial z} \right] \quad , (4)$$

Where $\mathbf{u} = (u, v)$ is the horizontal current velocity vector; w is the vertical current velocity, ϕ is the geopotential; $\mathcal{H} = kD$, k is the wave number, D is the wave-average thickness of the water column; f is the Coriolis parameter, \tilde{z} is the unit vector in the vertical direction; γ is the viscous parameter; a_i is the sea ice concentration; $\boldsymbol{\tau}_{aw}$ is the wind stress over the ocean; $\boldsymbol{\tau}_{wi}$ is the ocean-ice interfacial stress; $\mathbf{J} = -\tilde{z} \times \mathbf{u}^{st} ((\tilde{z} \cdot \nabla_{\perp} \times \mathbf{u}) + f) - w^{st} \frac{\partial \mathbf{u}}{\partial z}$ is the horizontal vortex force, \mathbf{u}^{st} and w^{st} are the horizontal and vertical stokes velocity, respectively; \mathbf{F}^w is the wave-induced nonconservative forces; g is the gravity acceleration; ρ and ρ_0 are the ocean density and reference density, respectively; $K = \mathbf{u}^{st} \frac{\partial \mathbf{u}}{\partial z}$; c is the tracer (i.e., temperature, salinity); κ is the Bernoulli head; \mathcal{E} is the wave-induced tracer diffusivity.

Ice model:

$$100 \quad \rho_i m_i \left(\frac{\partial \mathbf{u}_i}{\partial t} + \mathbf{u}_i \nabla_{\perp} \mathbf{u}_i \right) = -\rho_i (\nabla_{\perp} \phi + f \tilde{z} \times \mathbf{u}_i) + a_i \boldsymbol{\tau}_{ai} - a_i \boldsymbol{\tau}_{wi} + \mathbf{F}_i + a_i \mathbf{F}_r \quad , (5)$$

$$\frac{\partial a_i}{\partial t} + (\mathbf{u}_i \cdot \nabla_{\perp}) a_i = 0; \quad (0 \leq a_i \leq 1) \quad , (6)$$

$$\frac{\partial m_i}{\partial t} + (\mathbf{u}_i \cdot \nabla_{\perp}) m_i = 0; \quad m_i = a_i h_i \quad , (7)$$

Where $\mathbf{u}_i = (u_i, v_i)$ is the horizontal sea ice velocity vector; ρ_i , a_i , m_i and h_i are the density, concentration, mass and thickness of the sea ice, respectively; $\boldsymbol{\tau}_{ai}$ is the wind stress over the sea ice; \mathbf{F}_i is the internal stress vector of sea ice; \mathbf{F}_r is the radiative stress vector of sea ice, which is resulted from wave energy attenuation.

Wave model:

$$\frac{\partial \mathbf{k}}{\partial t} + \mathbf{c}_g \cdot \nabla_{\perp} \mathbf{k} = -\mathbf{k} \cdot \nabla_{\perp} \bar{\mathbf{U}} \pm \frac{k \rho_i}{\rho} \frac{\sqrt{gk}}{2(1+B_0 k)^{\frac{3}{2}}} \cdot \nabla_{\perp} m_i \quad , (8)$$

$$\frac{\partial \Lambda}{\partial t} + \nabla_{\perp} \cdot (\mathbf{c}_g \Lambda) = -(1 - a_i) \frac{\epsilon_b}{\omega_0} - a_i \alpha c_g \Lambda \quad , (9)$$

Where k and \mathbf{k} are the amplitude and the vector of the wave number, respectively; c_g and \mathbf{c}_g are the amplitude and the vector of the group velocity, respectively; $\bar{\mathbf{U}}$ is the depth-averaged ocean velocity vector; $B_0 = (\rho_i / \rho) m_i$; Λ is the wave action; ϵ_b is the wave dissipation rate due to breaking in the open ocean; ω_0 is the wave intrinsic frequency; and α is the wave energy spatial decay rate as it propagates through the ice field.

While the simulated eddy genesis process represents an idealized scenario, the sensitivity experiments are configured using background conditions (mean flow, stratification, wave characteristics, and sea ice properties) derived from reanalysis data.

115 The model was configured for a 200 km x 100 km domain with a horizontal resolution of 0.5 km, which is sufficient to resolve mesoscale eddy evolution. The grid comprises 40 levels in the vertical direction, with a total depth of 300 m. Vertical grid stretching is applied, with the finest resolution concentrated near the ocean surface and 7 levels in the upper 10 meters



of the water column. Open boundary conditions are imposed at the eastern and western boundaries, and north-south periodic boundaries are employed in the simulation.

120 2.3 Analysis method

Energy estimate was employed to analyze the numerical simulation result. Following Dai et al. (2019), the mean kinetic energy (MKE) is defined as $\bar{q} = \frac{1}{2} \bar{u}_i \bar{u}_i$, and the eddy kinetic energy (EKE) is defined as $q' = \frac{1}{2} \overline{u'_i u'_i}$, where $(u_1, u_2, u_3) = (u, v, w)$ and $u_i = \bar{u}_i + u'_i$. Since both the initial field and the external forcing are uniformed in the y direction. We define, $\bar{u}_i = \frac{1}{y_n - y_0} \int_{y_0}^{y_n} u_i dy$ as the mean velocity, while u'_i is the turbulent velocity. The mean available potential energy (MAPE) is defined as $\bar{Q} = \frac{1}{2} \bar{b} \cdot \bar{b} / \frac{\partial [b]}{\partial z}$, and the eddy available potential energy (EAPE) is defined as $Q' = \frac{1}{2} b' \cdot b' / \frac{\partial [b]}{\partial z}$, where $b = g \frac{\delta \rho}{\rho_0}$ is the buoyancy, g is gravity acceleration, $\delta \rho = \rho - \rho_0$, ρ is the water density, and ρ_0 is the water density reference. $b(x, y, z, t) = [b](z, t) + b^*(x, y, z, t)$, $[b] = \frac{1}{(y_n - y_s)(x_w - x_e)} \int_{y_s}^{y_n} \int_{x_w}^{x_e} b dx dy$ is the background buoyancy, $b^*(x, y, z, t) = \bar{b}(x, z, t) + b'(x, y, z, t)$, $\bar{b} = \frac{1}{(y_n - y_0)} \int_{y_0}^{y_n} b^* dy$ is defined as the mean buoyancy along the y direction, and b' is the turbulent buoyancy. In accordance with Nauw et al. (2006), Thomas (2008) and Olbers et al. (2012), the Brunt–Vaisala frequency is defined as $N^2 = \frac{\partial [b]}{\partial z}$, the Rossby radius is defined as $R_d = \frac{NH}{\pi}$, and the Burger number is defined as $Bu = \frac{NH}{fL}$, where f is the Coriolis parameter and H and L are the water depth and the horizontal scale length of the eddy, respectively.

3 Ocean-ice-wave interactions and eddy genesis

3.1 The influence of current and stratification

The reanalysis data revealed an anticyclonic eddy with a diameter of approximately 40 km (Fig. 1b, green crossing), which nearly overlapped with the observed eddy (Fig. 1b, red star), at the ice edge (Fig. 1b, pink line) of the Fram Strait. However, sea ice was not as that present in the SAR image, which may have resulted from the coarse resolution failing to reproduce the granularity of the sea ice. The anticyclonic eddy is located on the northwestern side of the EGC (Fig. 1b, vector), thus barotropic instability could contribute to eddy genesis. By tracing the eddy's evolution, we revealed that this eddy originated on September 12, 2020 (Fig. 2a, green crossing), when it exhibited a small negative vorticity and was located in a weaker branch of the EGC (Fig. 2a, vector). At this point in time, it was not yet an eddy, since its vorticity (ζ_f , Fig. 2a, shading) was only -0.15 and no more than 0.1 smaller than the surrounding vorticity. In the following days, the eddy increased in mean flow (Fig. 2b, shading) and then weakened due to eddy splitting on September 20, 2020 (Fig. 2c, shading). After splitting, the eddies continued to grow from September 24 (Fig. 2d, shading) to October 4, 2020, with the second eddy strengthening (September 24 to October 4) and outgrowing the first (September 12 to 18). Jet strengthening is a significant feature. Before



145 September 12, the main body of the EGC (Fig. 2e, white dotted line) was located hundreds of kilometers east of the eddy (Fig. 2e, green crossing). However, during the following days, the upstream branch flow, where the eddy was located, strengthened (Fig. 2f, g; shading and white dotted line). After September 24, the strength of the branch (Fig. 2h, shading), where the eddy (Fig. 2h, green crossing) was located, was much stronger (0.24 m/s) than it was before September 15 (Fig. 2e, f, shading, 0.1 m/s); furthermore, it was closer to the main body of the EGC (Fig. 2h, white dotted line). The consistency
150 between the jet strength and the eddy strength suggested the contribution of barotropic instability during eddy evolution. At beginning, we considered wind stress (τ_{aw}) and ocean-ice interfacial stress (τ_{wi}) as the primary mechanisms to the jet variation ($\frac{\partial \mathbf{u}}{\partial t}$), since vortex force (\mathbf{J}) and nonconservative wave force (\mathbf{F}^w) are relatively small in the open ocean (Dai et al. 2019). We first analyzed surface wind stress over the current ($\tau_{aw} = C_{aw} |\mathbf{u}_a| \mathbf{u}_a$), which is mainly determined by the surface wind (\mathbf{u}_a). To illustrate the total contribution of the surface wind, we integrate the surface wind from the earlier time
155 point to the later time point ($\delta \mathbf{u} = \mathbf{u}_{t2} - \mathbf{u}_{t1} = \int_{t1}^{t2} \tau_{aw} dt$, Fig. 2f-h, vector). For example, vectors in Fig. 2f, Fig. 2g, and Fig. 2h indicate the surface winds integrated over September 13 to 15, September 16 to 20, and September 21 to 24, respectively. Surface winds appeared relatively homogenous during these periods, which cannot explain the sharp increase in the current at the eddy location. The second hypothesis is ice acceleration induce current acceleration via ocean-ice interfacial stress (τ_{wi}). McPhee (1975) suggested that currents under the ice accelerate much faster than those in the open
160 ocean due to the higher efficiency of momentum transfer between the air and ice than between the air and ocean, which means the amplitude of current acceleration follows the amplitude of ice concentration, given the same wind forcing. However, this hypothesis also fails to explain the faster acceleration observed at the ice edge (Fig. 2, pink line) than in the inner ice zone (Fig. 2e-f, shading). In addition, a third hypothesis is proposed and may well fit the observation: most wave energy dissipates ($a_i a c_g \Lambda$) at ice edge, and the momentum is transferred into the ice via radiative force (\mathbf{F}_r), which is in turn
165 transferred into the current via ocean-ice interfacial stress. As a result, wave-ice interaction-induced current acceleration reach its maximum at the ice edge (Dai et al 2019, Thomson et al 2021). Before we describe the story, we need make two tips. First, Mercator Center provide the wave information, although they seem to neglect the wave in the ice-covered region (Fig. 3, white color) instead of describing how the wave propagates in the ice zone in the model. Second, different resolutions between the ice model ($1/8^\circ$) and wave model (2°) entail that the ice zone exhibits a smaller area in the wave
170 model (Fig. 3, white color) than in the ice model (Fig. 3, pink line). Between September 20 to October 1, the sea ice increases and expands to the southeast. Sea ice covered the EGC at a high latitude (78.5°N) on September 20, and the EGC strengthened there. After September 28, the sea ice covered the branch flow (Fig. 3d, the green crossing is located in the non-wave region, which means the branch of the EGU is under the sea ice), which helped the branch flow grow and become comparable in size to the main body of the EGC. During this period, the wave continues propagating toward the ice zone and
175 disappears at the ice edge. The sea ice expands toward the eddy location, and the wave strength becomes much stronger after September 21 (Fig. 3c, d, shading). We think the ice-edge current acceleration is captured by the reanalysis data because of the using of data assimilation, since wave-ice interactions were not described in the model.



180 Nonetheless, baroclinic instability is also detected during the same period. During the autumn, sea ice increases and expands against the coast and higher latitudes (Fig. 4a, b; pink line) due to temperature cooling. Sea ice formation induces salinity rejection, which enhances salinity (Fig. 4, shading) in the ice-covered region; however, the salinity is still lower than that in the open ocean. During sea ice expansion, denser water is produced in the ice-covered region due to ice formation and salinity rejection. The salinity in the EGC is relatively homogenous during the ice retreat period, and the increased salinity in the ice-covered region leads to the growth of the ocean front (Fig. 4e-h, shading). Based on the preceding description, baroclinic instability may not be the primary reason for eddy evolution. During the ice expansion period, the front grows
185 (Fig. 4e-h, shading) due to denser water formation, and the eddy strengthens. If the front is characterized by baroclinic instability, the front strength should always exhibit the opposite phase as the eddy strength.

3.2 Wave-ice interaction, jet and eddies

Although the data analysis seem to support the third hypothesis, there are still three primary issues that the reanalysis data fail to reproduce: (1) the distributions of waves, ice and current are not unified due to different resolutions of the models, (2)
190 the role of waves and ice in determining the jet strength remains uncertain due to the description of the mechanism included in the models, and (3) whether the ocean features can produce jet and eddies based on the third hypothesis. To address these three issues, a coupled ocean-ice-wave model with a fine horizontal resolution (500 m) is employed in this study. To eliminate the contribution of baroclinic instability, temperature, salinity and density are set to be horizontally uniform, and stratification is set to inhibit vertical motion. Two sensitivity experiments are completed with the ROMS-SSIM. Experiment
195 1 (EXP1) features only a meridional jet ($v_{max}=0.48$ m/s; Fig. 5a, shading; which is 0.2 - 0.6 m/s from the 200-m layer to the sea surface in the reanalysis data) along the ice edge in the domain, which is also the control experiment. In experiment 2 (EXP2), the meridional jet is also set along the ice edge as that in EXP1. In addition, a continuous wave ($k=0.021$ m⁻¹; wave length of 300 m), which propagates with an incident angle of 73.3° ($k_y/k_x=10/3$) toward the ice edge, is set at the eastern boundary of this domain. Constant waves are set with a significant wave height of 1.5 m and a wave action of 25.0, since the
200 wave height in the reanalysis data ranges from 0 to 3.3 m (mean value is 1.5 m), the wave energy at the boundary is approximately 5-20 Jm⁻² (Fig. 3, shading), and wave period is 2.2-11.62 s⁻¹, thus indicating that the wave number and wave length are 0.001-0.021 m⁻¹ and 300-6000 m, respectively. We choose shorter wavelengths in the numerical simulations, and we discuss the consequences of replacing the shorter wavelength with a longer wavelength in the next section. The marginal ice zone (sea ice concentration (a_i) is between 0.15 and 0.7) is 5 km (5 km is approximately the grid length in the reanalysis
205 data) along the x direction, whereas the ice thickness is horizontally uniform (1.2 m, which is 0.4 to 1.2 m in the reanalysis data). Surface wind is set to be horizontally uniform (speed= 1 m/s) as in the reanalysis data (Fig. 2g, h, vector). The direction of the wind is the same as that of the jet in the initial field. The two experiments span 30 days, which is longer than the timeframe considered in the reanalysis data (23 days, September 12 to October 4), since a vorticity center was already present on September 12.



210 In EXP1, the story is quite simple. Due to a strong velocity shear between the meridional jet and surrounding flow (Fig. 5a, shading), mesoscale eddies ($\frac{\zeta}{f} \sim 0.1$, Fig. 5b, shading) were produced via barotropic instability after 30 days of integration. In contrast, EXP2 is employed to verify the third hypothesis, which is wave-ice interaction leading along ice-edge jet. When the continuous waves are set at the eastern boundary (EXP2), they propagate toward the ice zone. According to equation (8), wave refraction mainly occurs in the x-direction, and k_x (wave number in the x direction, Fig. 6a, red line) increases at the

215 ice edge due to the ice mass gradient in the x-direction ($\frac{\partial m_i}{\partial x}$, Fig. 6a, black line). Meanwhile, wave energy (Fig. 6a, green line) dissipated rapidly at the ice edge due to wave attenuation rate ($a_i a c_g \Lambda$); which induce the energy being transferred from wave to the sea ice via radiative stress (Fr). Since the incident angle is 73.3° ($ky/kx=10/3$), most energy is transferred in the along-ice-edge direction. There is energy transferred into the x-direction (cross-ice-edge direction). In addition, the meridional velocity increases the zonal velocity via the Coriolis force. As a result, there is significant

220 acceleration of sea ice in the x-direction, especially at ice edge, which pushes the whole ice zone move westward. On the other hand, ice edge moves faster than the inner ocean, there is ice convergence at the new ice edge, the transition zone (0.15-0.7) become narrower (Fig. 6a, blue line). Because of ocean-ice interfacial stress, there is also current acceleration beneath the sea ice. On day 18, the ice edge appears at $x=16$ km, so are the meridional jet both in the sea ice and in the ocean ($v=1.1$ m/s; Fig. 5c; shading). Since wave-ice interactions and additional acceleration occurred at the sea surface, the jet

225 strength reached its maximum in the upper layer and became much weaker in the lower layers (Fig. 5e, shading). Notably, the meridional jet in the initial field disappeared in EXP2, while the new jet was located at the ice edge (Fig. 5c, shading). Due to stronger velocity shear in the jet (2.5 times of that in EXP1), stronger mesoscale eddies ($\frac{\zeta}{f} \sim 1$, Fig. 5d, shading) were produced via barotropic instability after 30 days of integration in EXP2. Since the density is homogenous in both EXP1 and EXP2, there is nearly no potential energy available for the eddy (EAPE, Fig. 6b, c, black line) remained small. The kinetic

230 energy of the eddy (EKE, Fig. 6b, c, green line) is mainly transferred from the mean kinetic energy (MKE, Fig. 6, purple line) via Reynolds stress work (RSW, blue line). In EXP1, the MKE (Fig. 6b, purple line) continued to decrease and was transferred into EKE (Fig. 6b, green line). In EXP2, the MKE (Fig. 6c, purple) initially increased due to wave energy dissipation (Fig. 6a, green line). As a result, the eddies in EXP2 are much stronger than those in EXP1. Due to the ocean-ice interfacial stress, the ice floes move following the eddy activity. As a result, there is meandering in the ice edge of the

235 marginal ice zone (Fig. 5f, shading), as observed by the satellite (Fig. 1a).

4 Conclusion and discussion

In this study, typical eddy generation, as detected by satellite, in the Fram Strait was investigated on the basis of reanalysis data. The process is described as follows: the EGC moves equatorward in the Fram Strait with high speed in the main body and lower speed in the branch. In the branch, a small velocity shear can only produce weak eddies, which easily disappear

240 via eddy splitting. In the autumn, the sea ice expands against the coast and approaches the EGC. Simultaneously, surface



waves propagate freely in the open ocean with a low dissipation rate. When waves propagate into the ice zone, most of the corresponding energy is dissipated rapidly at the ice edge due to wave-ice interactions. This energy is transferred into the sea ice via radiation stress and is alternatively transferred into the ocean via ocean-ice interfacial stress. As a result, the current accelerates, thus leading the speed of the branch to become comparable with that of the main body of the EGC; it also
245 strengthens eddy activity via larger velocity shear and baroclinic instability.

In this study, we discussed the eddy genesis process in further depth and in more ways than previous studies have achieved. First, we solved three issues outlined in the introduction. (1) Wave-ice interactions constitute a significant contributor to the EGC. (2) Wave-ice interactions produce eddies via barotropic instability, which was first proposed on the basis of numerical simulations in previous studies; however, this point has hitherto remained entirely theoretical (Dai et al. 2019). Subsequently,
250 Thompson et al. (2021) observed that wave-ice interactions led to jets in the Chukchi Sea. Employing satellite observations and reanalysis data, this study successfully documented the complete process within the Fram Strait. (3) Wave energy, the extent of the marginal ice zone, and water depth are identified as critical constraints that govern the occurrence of this mechanism. In Chukchi Sea, the water depth is small, which may largely decrease the jet strength via bottom drag and hardly produce visible eddies via barotropic instability (Zhang et al. 2020). At higher latitudes, wave energy is typically insufficient
255 to trigger this mechanism, rendering it unobservable. With these three constraints, the wave-ice interaction induce eddy activity may also be found in Barents-Kara Sea in cold season, when there is strong wave energy, marginal ice zone and large water depth.

Second, we employed a shorter wavelength and a larger incident wave in the numerical simulations. When the wavelength increase (smaller wavenumber), the energy dissipation rate of the wave decreases, which decreases the strength of the jet and
260 the mesoscale eddy (Zhang et al. 2020). When the incident angle decreases, more energy is transferred into the cross-ice-edge direction, and the jet and eddy weaken (Zhang et al. 2020). Thus, we chose good conditions to produce a stronger mesoscale eddy, which led to much stronger eddies than were observed in the reanalysis data, despite the fact that we started with zero vorticity conditions.

Third, baroclinic instability is an important mechanism that produces mesoscale eddies in the Arctic. However, the salinity is
265 lower closer to the ice zone in the autumn in the Fram Strait. When sea ice formation and salinity rejection occur in the ice zone followed by ice zone expansion, the salinity difference between the ice zone and open ocean is first erased. The ocean front subsequently begins to appear, which contributes little to eddy generation in comparison with the barotropic instability mechanism.

Although eddy activity displays a synoptic scale event, the accumulation of eddy activities may also contribute significant
270 influence on climate. For example, more than 1000 eddies are found in Fram Strait and Barents-Kara Sea every year. Eddy activity may induce additional vertical motion. On the other hand, Fram Strait and Barents-Kara Sea are also one of the key regions that the seasonal heat storage (SHS) formation / release occurs (Wu and Dai, 2025). In summer, there are a lot of solar radiation arrive the Arctic surface and is absorbed by ocean. In cold season, part of the energy is released from the ocean and warms the atmosphere. This part of energy is called SHS, which is also the key mechanism to determine the



275 Arctic warming from summer to winter (Dai, 2021; Dai et al. 2022). How the additional vertical motion contributes to SHS and Arctic warming will be studied in our future work.

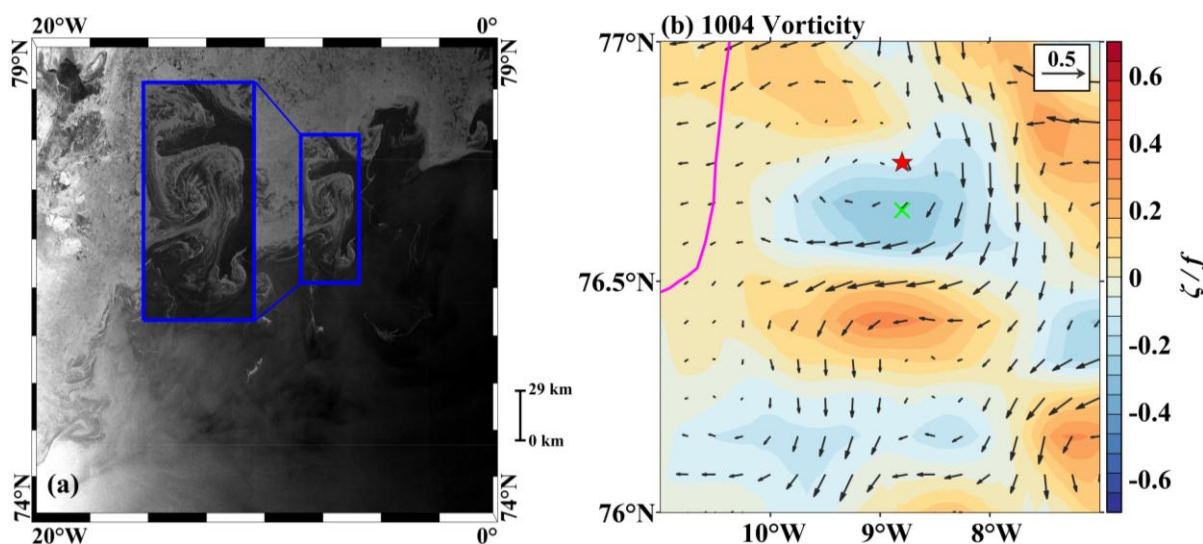
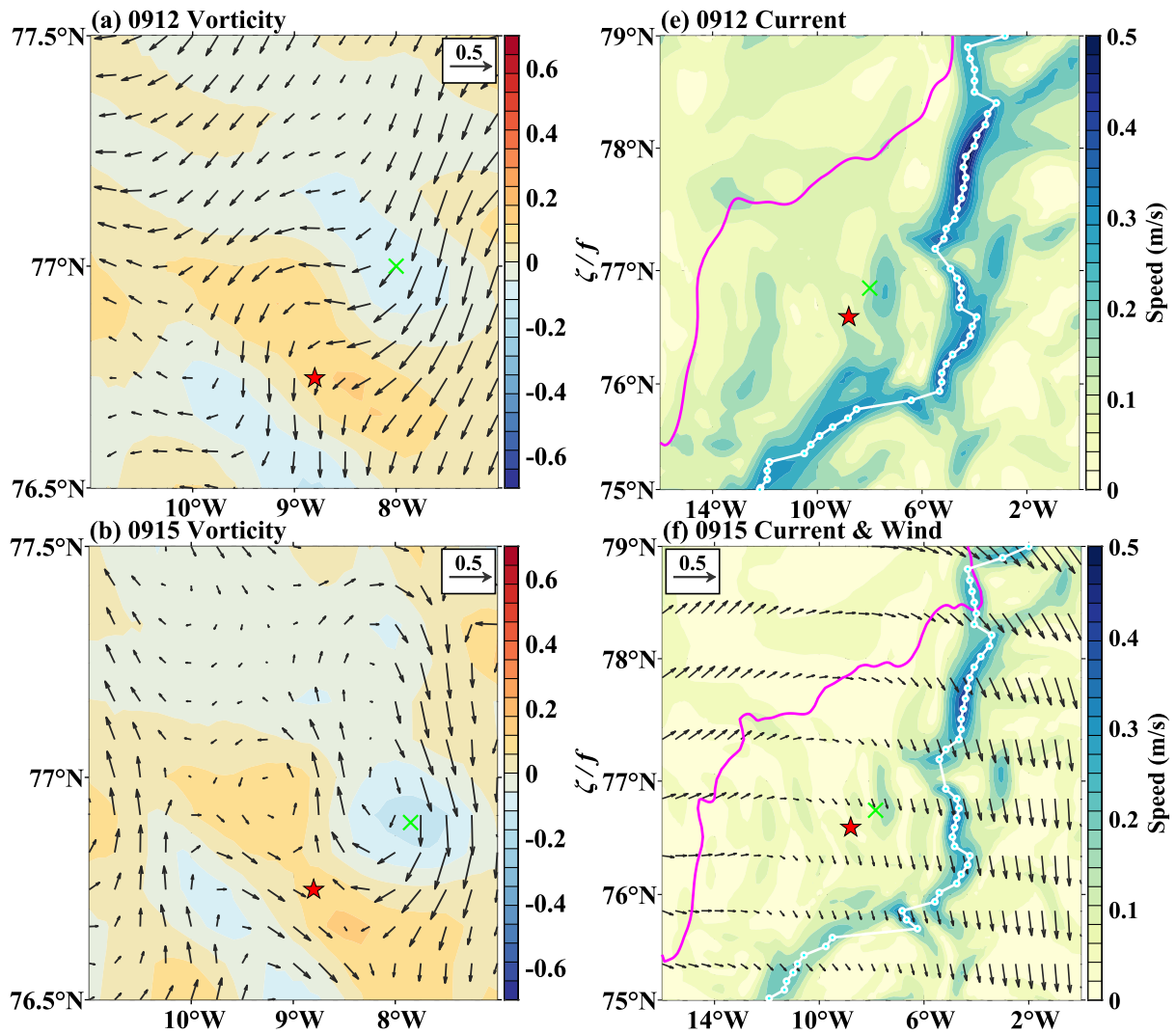


Figure 1: Mesoscale eddy captured by satellite observation and reanalysis data.

280 (a) Part of the Fram Strait on October 4, 2020, is shown with the SAR image, and the mesoscale eddy region is magnified in the blue rectangle. The SAR image is produced by SNAP after the Sentinel-1 data was downloaded from the website <https://search.asf.alaska.edu/#/>. In the SAR image, the open ocean is dark gray, while the ice is much brighter; i.e., the white color north of the mesoscale eddy is the ice zone. The diameter of the eddy is defined as the horizontal scale of the eddy, while the eddy is defined as the ice floes acting as traces mirroring the ocean circulation. (b) Vertical vorticity (ξ/f , shading, unit: nondimensional), current (vector, unit: m/s), and ice edge ($a_i = 15$, pink line, unit: %) at the sea surface on October 4, 285
2020, are shown. Green crossing and the red star indicate the eddy location in the reanalysis data and the satellite observation, respectively.



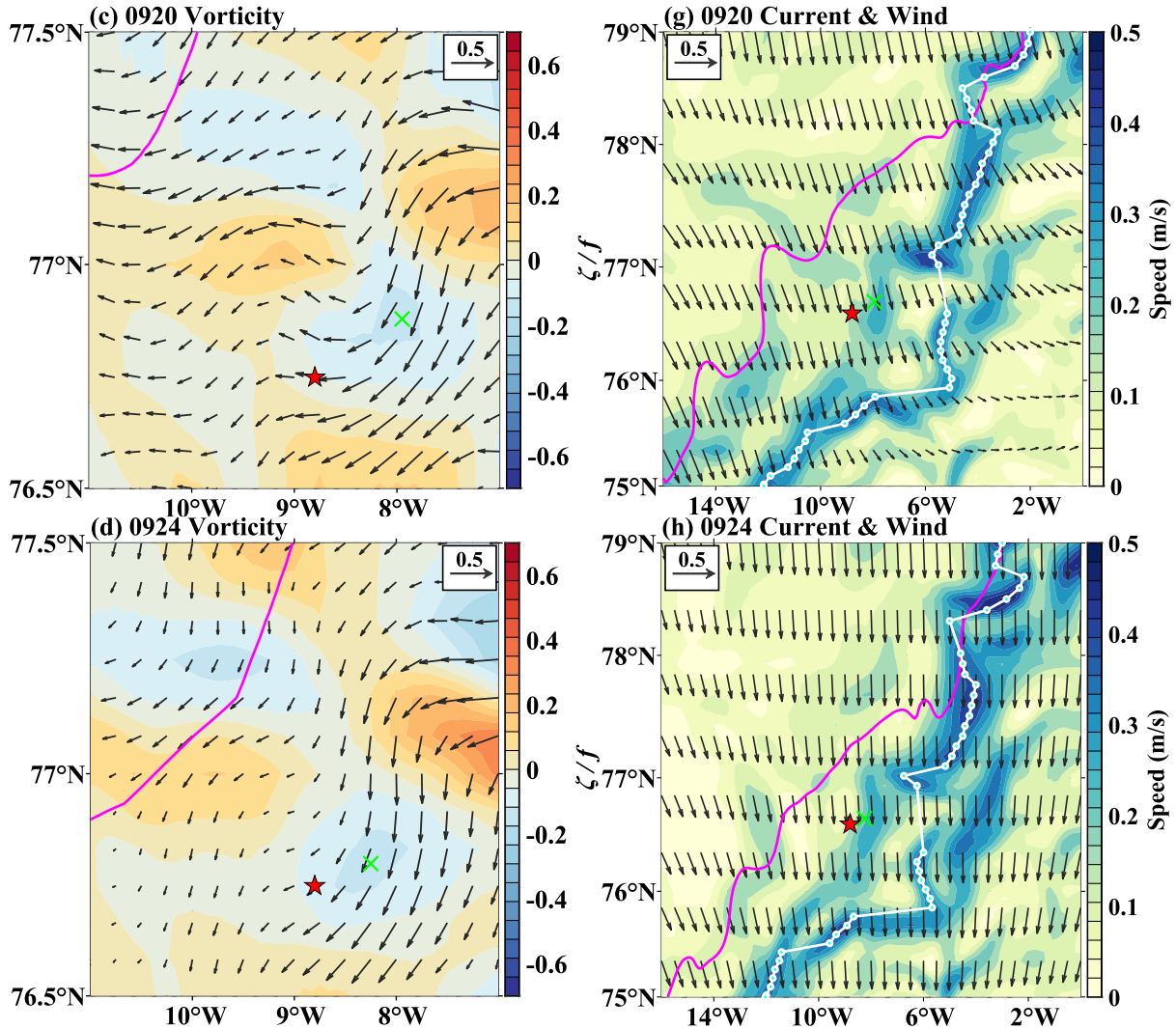
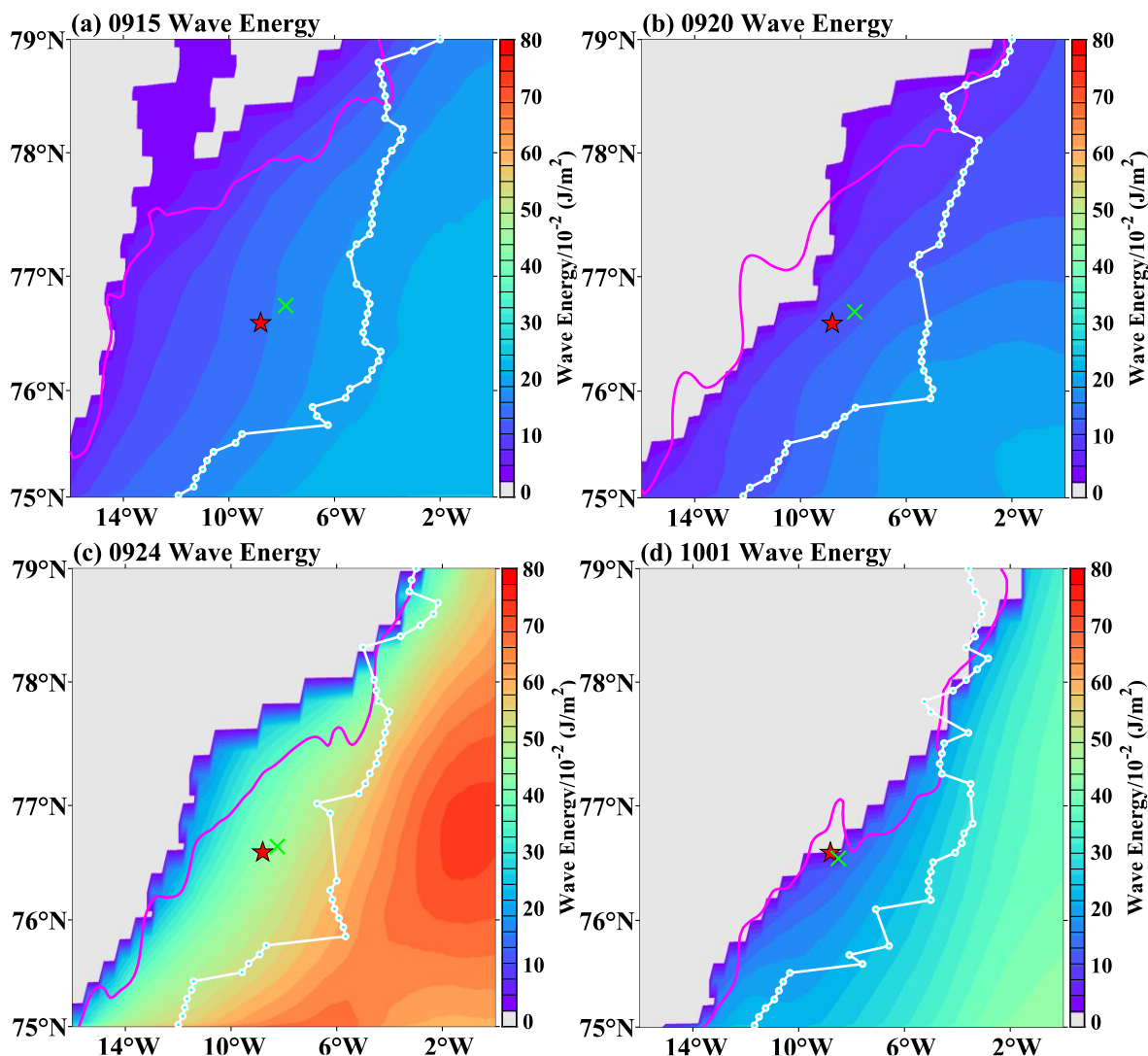


Figure 2: Surface wind and surface current in reanalysis data.

The vertical vorticity (ζ/f , shading, unit: nondimensional), the current (vector, unit: m/s), ice edge (ai = 15, pink line, unit: %) and target eddy location (green crossing) are the reanalysis data for September (a) 12, (b) 15, (c) 20, and (d) 24, 2020. Red star indicates the eddy location on October 4 in the satellite observation. The current speed (unit: m/s) and the axis of the jet stream (the speed maximum at each latitude) are presented as shading and white dotted lines in (e)-(h), respectively. Surface wind averaged over September 13 to 15, September 16 to 20, and September 21 to 24 are presented as vectors in (f), (g) and (h), respectively. The green crossings and red stars have the same meanings as in (a)-(d).

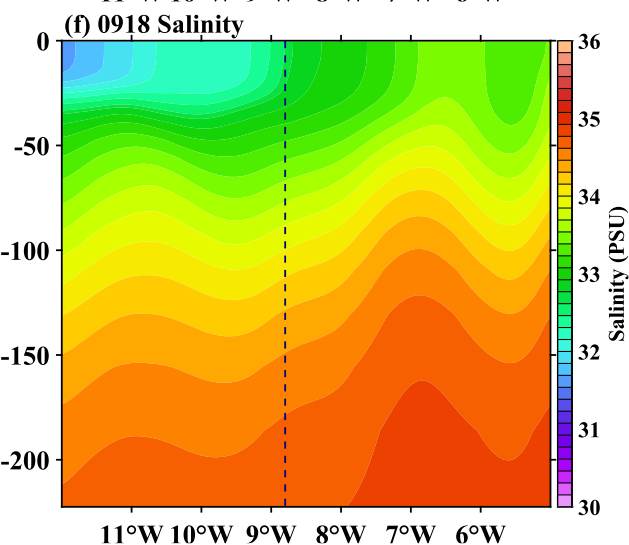
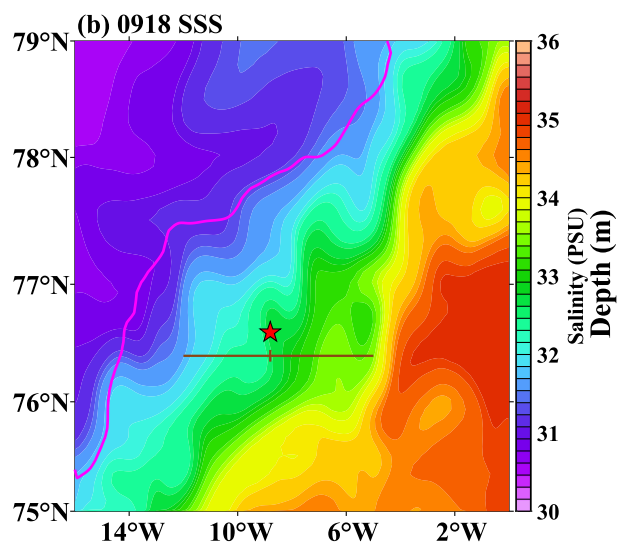
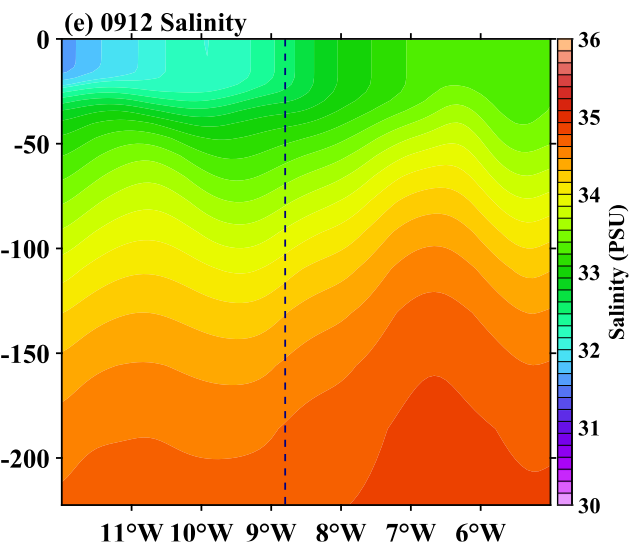
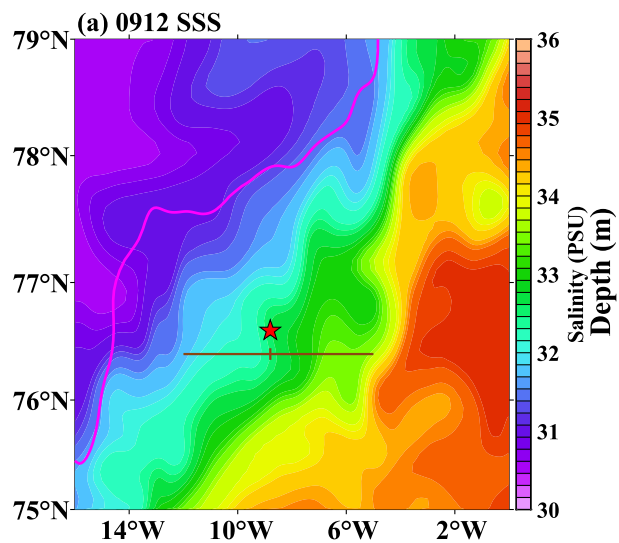


300

Figure 3: Surface wave, sea ice and jet in reanalysis data.

The wave energy (shading, unit: J/m^2) and ice edge ($a_i = 15$, pink line, unit: %) averaged over September 13 to 15, September 16 to 20, September 21 to 24, and September 25 to October 1 are shown in (a), (b), (c), and (d), respectively. The eddy location and the axis of the jet stream (the speed maximum at each latitude) on September 15, 20, 24 and October 1 are presented as green crossing and white dotted lines in (a), (b), (c) and (d), respectively. Red star indicates the eddy location on October 4 in the satellite observation. Gray shading indicates the ice zone (wave information is missing value) in wave model.

305





310

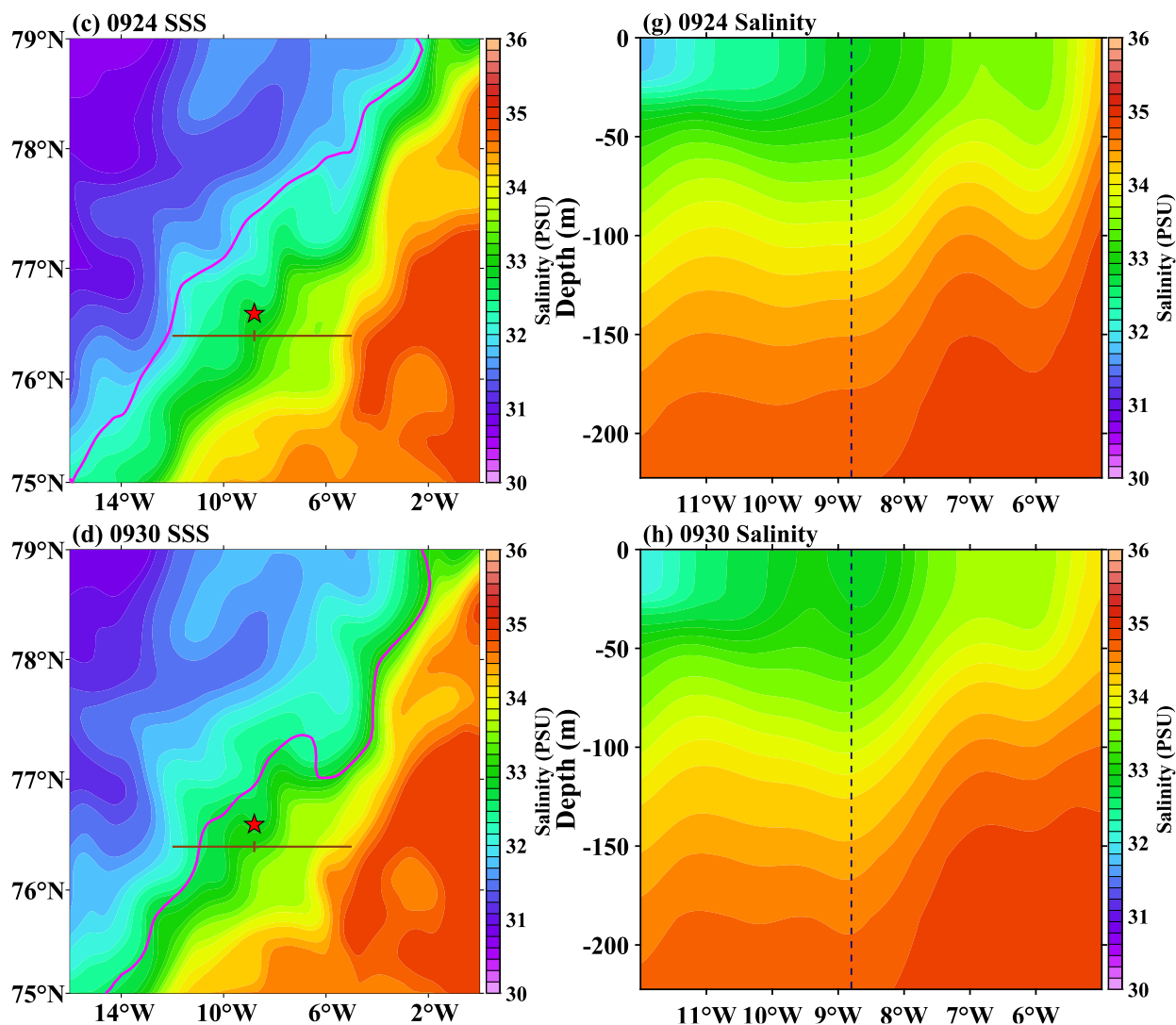


Figure 4: Salinity in reanalysis data.

Sea surface salinity (SSS, shading, unit: PSU) and the ice edge ($ai = 15$, pink line, unit: %) on September 12, 18, 24, and 30 are shown in (a), (b), (c), and (d), respectively. Selected sections to plot the vertical profile in (e)-(h) are shown as brown crossing. Red star indicates the eddy location on October 4 in the satellite observation. Green crossings indicate where the vertical profiles are taken. The vertical profiles of salinity (latitude=76.5 N; shading; unit: PSU) on September 12, 18, 24, and 30 are shown in (e), (f), (g), and (h), respectively. Black dash lines indicate the longitude of the eddy location on October 4.

315

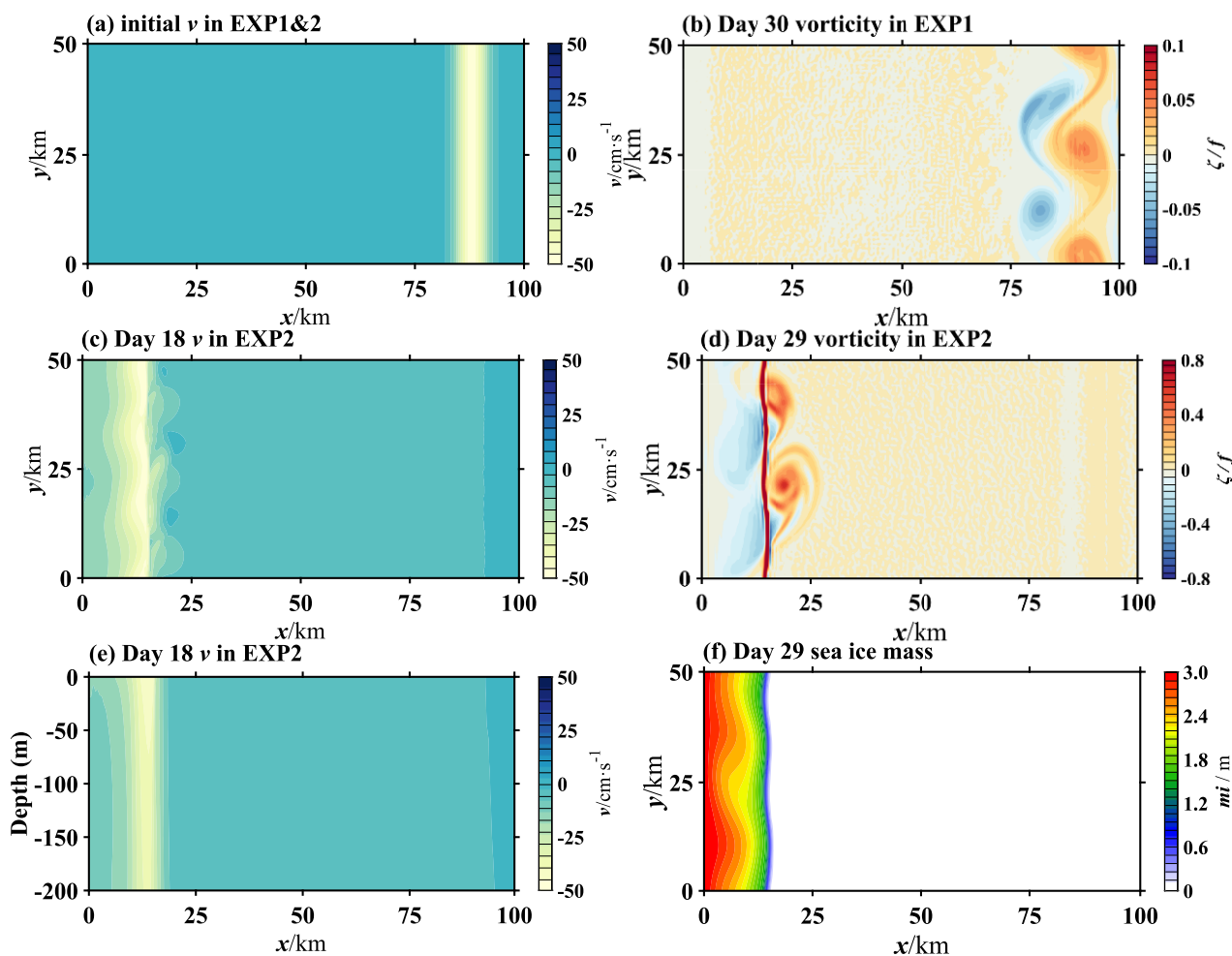


Figure 5: Mesoscale eddies reproduction with numerical simulations.

The (a) initial sea surface meridional velocity (v , shading, unit: m/s) and (b) vorticity (ζ/f , shading, unit: nondimensional) on day 30 from EXP1 are shown. The (c) sea surface meridional velocity (v , shading, unit: m/s), and (e) vertical profile of meridional velocity (v , shading, unit: m/s) on day 18 from EXP2 are shown. The (d) vorticity (ζ/f , shading, unit: nondimensional) and (f) sea ice mass (m_i , shading, unit: m) on day 29 from EXP2 are also illustrated.

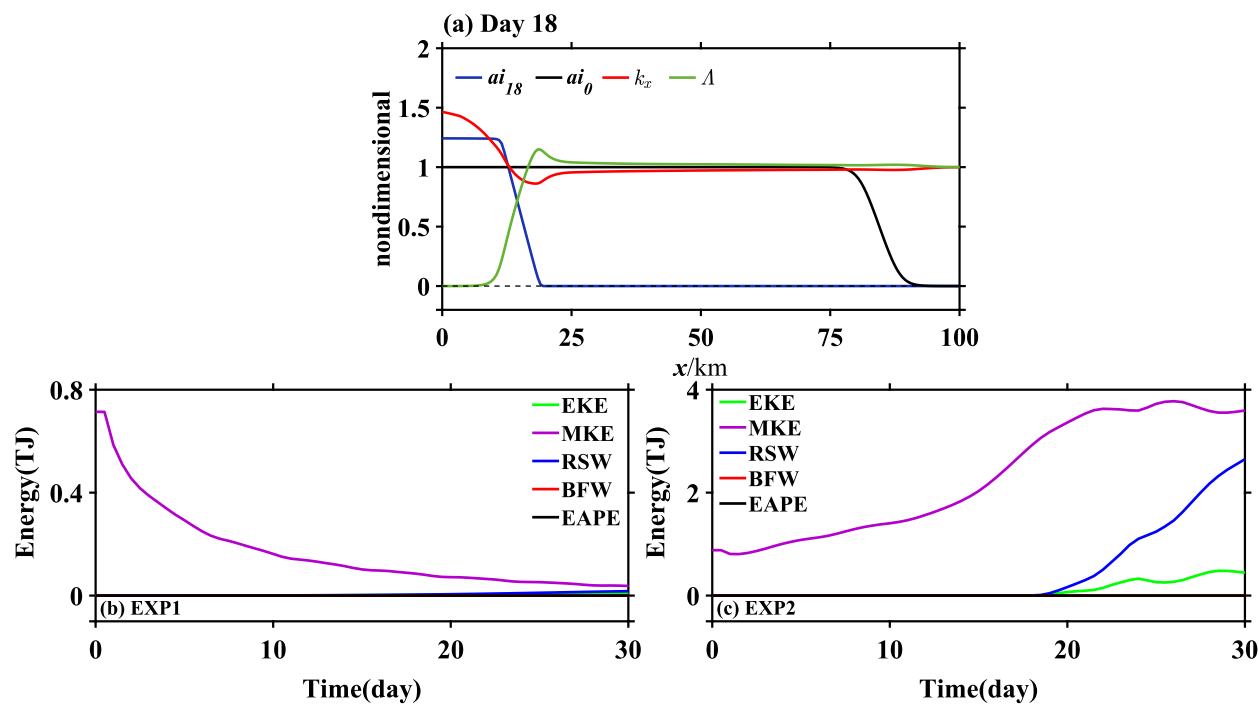


Figure 6: Energy budget estimate with numerical simulations.

330 (a) Wave number in the x-direction (k_x , red line, unit: nondimensional), wave energy (Λ , green line, unit: nondimensional), and sea ice concentration (a_i , blue line, unit: nondimensional) on day 18, and initial sea ice concentration (black line, unit: nondimensional) from EXP2 are shown. Energy evolution (unit: TJ= 10^{12} J) in (b) EXP1 and (c) EXP2 are shown. The blue line indicates the kinetic energy (KE) transferred from the mean flow KE (MKE, purple line) to the eddy KE (EKE, green line), which is the result of time integration of the Reynolds stress work (RSW). The red line indicates the energy transferred from the eddy available potential energy (EAPE, black line) to the EKE, which is the result of time integration of the buoyancy flux work (BSW) on the eddy.

335

References

Aksenov, Y., Karcher, M., Proshutinsky, A., Gerdes, R., de Cuevas, B., Golubeva, E., Kauker, F., Nguyen, A. T., Platov, G. A., Wadley, M., Watanabe, E., Coward, A.C. and Nurser, A. J. G.: Arctic pathways of Pacific Water: Arctic Ocean model intercomparison experiments. *J. Geophys. Res. Oceans*, 121, 27–59, doi:10.1002/2015JC011299, 2016.

340 Bashmachnikov, I. L., Kozlov, I. E., Petrenko, L. A., Glok, N. I. and Wekerle, C.: Eddies in the North Greenland Sea and Fram Strait from satellite altimetry, SAR and high-resolution model data. *J. Geophys. Res.-Oceans*, 125, e2019JC015832, doi:10.1029/2019JC015832, 2020.

Dai, H., Cui, J., and Yu, J.: Revisiting mesoscale eddy genesis mechanism of nonlinear advection in a marginal ice zone.

345 *Acta Oceanol. Sin.*, 36, 14–20, doi:10.1007/s13131-017-1134-8, 2017.



- Dai, H., Li, T., Ding, J., and Yao, Y.: An ITP observed warm core eddy is produced by fresh water intrusion in the subsurface Beaufort Sea. *Estuarine, Coastal and Shelf Science*, 313, 109098, doi:10.1016/j.ecss.2024.109098, 2025.
- Dai, H., McWilliams, J. C. and Liang, J.: Wave-driven mesoscale currents in a marginal ice zone. *Ocean Modelling*, 134, 1-17, doi:10.1016/j.ocemod.2018.11.006, 2019
- 350 Dumont, D., Kohout, A. and Bertino, L.: A wave-based model for the marginal ice zone including a floe breaking parameterization. *J. Geophys. Res.-Oceans*, 116, C04001, doi:10.1029/2010JC006682, 2010
- Garric, G., Parent, L., Greiner, E., Drévillon, M., Hamon, M., Lellouche, J. M., et al. In Buch E., Fernandez, V., Nolan, G. and Eparkhina, D. (Eds.), Performance and quality assessment of the global ocean eddy-permitting physical reanalysis GLORYS2V4 operational oceanography serving sustainable marine development. Proceedings of the eight EuroGOOS international conference. 3-5 October 2017, Bergen, Norway (p. 516) [Dataset]. EuroGOOS (ISBN:978-2-9601883-3-2), 355 2018.
- Gula, J., Molemaker, M. and McWilliams, J. C.: Topographic generation of submesoscale centrifugal instability and energy dissipation. *Nature Communications*, 7, 12811, doi:10.1038/ncomms12811, 2016.
- Häkkinen, S.: Coupled ice-ocean dynamics in the marginal ice zones: upwelling/downwelling and eddy generation. *J. 360 Geophys. Res.-Oceans*, 91 (C1), 819-832, doi:10.1029/JC091iC01p00819, 1986
- Häkkinen, S.: Feedback between ice flow, barotropic flow, and baroclinic flow in the presence of bottom topography. *J. Geophys. Res.-Oceans*, 15, 3807–3820, doi:10.1029/JC092iC04p03807, 1987.
- Hersbach, H., Bell, B., Berrisford, P., Biavati, G., Horányi, A., Muñoz Sabater, J., Nicolas, J., Peubey, C., Radu, R., Rozum, I., Schepers, D., Simmons, A., Soci, C., Dee, D. and Thépaut, J-N: ERA5 hourly data on single levels from 1940 to present. 365 Copernicus Climate Change Service (C3S) Climate Data Store (CDS) [Dataset]. (Accessed on DD-MMM-YYYY)
- Hunkins, K. L.: Subsurface eddies in the Arctic ocean. *Deep Sea Research and Oceanography*, 21, 1017-1033, 2023.
- Iakovlev, N.G. (2018). Arctic Ocean modeling: The consistent physics on the path to the high spatial resolution. In: Velarde, M., Tarakanov, R., Marchenko, A. (eds) *The Ocean in Motion*. Springer Oceanography. Springer, Cham. 1974
- Johannessen, J. A., Johannessen, O. M., Svendsen, E., Shuchman, R., Manley, T., Campbell, W. J., Josberger, E. G., 370 Sandven, S., Gascard, J. C., Olaussen, T., Davidson, K. and van Leer, J.: Mesoscale eddies in the Fram Strait marginal ice zone during the 1983 and 1984 Marginal Ice Zone Experiments. *J. Geophys. Res.-Oceans*, 92, 6754-6772, doi:10.1029/JC092iC07p06754, 1987.
- Josberger, E. G.: Sea ice melting in the marginal ice zone. *J. Geophys. Res.*, 88, 2841-2844, doi:10.1029/JC088iC05p02841, 1983.
- 375 Li, X., Wang, Q., Danilov, S., Koldunov, N., Liu, C., Müller, V., Sidorenko, D. and Jung, T.: Eddy activity in the Arctic Ocean projected to surge in a warming world. *Nature Climate Changes*, 14, 156-162, doi:10.1038/s41558-023-01908-w, 2024.
- Liu, A. K., Häkkinen, S. and Peng, C. Y.: Wave effects on ocean-ice interaction in the marginal ice zone. *J. Geophys. Res.-Oceans*, 98, 10,025-10,036, doi:10.1029/93JC00653, 1983.



- 380 Manley, T. O. and Hunkins, K.: Mesoscale eddies of the Arctic Ocean. *J. Geophys. Res.-Oceans*, 90, 4911-4930, doi:10.1029/JC090iC03p04911, 1985.
- Manucharyan, G. E. and Thomposon, A. F.: Submesoscale Sea Ice-Ocean Interactions in Marginal Ice Zones. *J. Geophys. Res.-Oceans*, 122, 9455-9475, doi:10.1002/2017JC012895, 2017.
- McWilliams, J. C., Restrepo, J. M. and Lane, E. M.: An asymptotic theory for the interaction of waves and currents in
385 coastal waters. *J. Fluid Mech.*, 511, 135-178, doi:10.1017/S0022112004009358, 2004.
- McWilliams, J. C.: Submesoscale currents in the ocean. *Proceedings of the Royal Society A*, 472, 20160117, doi:10.1098/rspa.2016.0117, 2016.
- McPhee, M. G.: Ice-ocean momentum transfer for the AIDJEX ice model. *AIDJEX Bull*, 29, 93-112, 1975.
- MIZEX Group: MIZEX East 83/84: The summer marginal ice zone program in the Fram Strait / Greenland Sea. *Eos*
390 *Transactions American Geophysical Union*, 67(23), 513–517, doi:10.1029/EO067i023p00513, 1986.
- Paquette, P. G. and Bourke, R. H.: Ocean Circulation and Fronts, Relate to ice melt-back in the Chukchi Sea. *J. Geophys. Res.-Oceans*, 86, 4125-4230, doi:10.1029/JC086iC05p04215, 1981.
- Shchepetkin, A. F. and McWilliams, J. C.: The regional oceanic modeling system (ROMS): a split-explicit, free-surface, topography-following-coordinate oceanic model. *Ocean Modelling*, 9, 347-404, doi:10.1016/j.ocemod.2004.08.002, 2005.
- 395 Squire, V. A.: Of ocean waves and sea-ice revisited. *Cold Regions Science and Technology*, 49, 110-133, doi:10.1016/j.coldregions.2007.04.007, 2007.
- Squire, V. A., Dugan, J. P., Wadhams, P., Rottier, P. J. and Liu, A. K.: Of ocean waves and sea ice. *Annual Review of Fluid Mechanics*, 27, 115-168, doi:10.1146/annurev.fl.27.010195.000555, 1995.
- Sutherland, D. A. and Pickart, R. S.: The East Greenland Coastal Current: Structure, variability, and forcing. *Progress in*
400 *Oceanography*, 78, 58-77, doi:10.1016/j.pocean.2007.09.006, 2008.
- Haine, T. W. N., Curry, B., Gerdes, R., Hansen, E., Karcher, M., Lee, C., Rudels, B., Spreen, G., de Steur, L., Stewart, K. D. and Woodgate, R.: Arctic freshwater export: Status, mechanisms, and prospects. *Global and Planetary Change*, 125, 13-35, doi: 10.1016/j.gloplacha.2014.11.013, 2015.
- Thomson, J., Lund, B., Hargrove, J., Smith, M. M., Horstmann, J. and MacKinnon, J. A.: Wave-driven flow along a compact
405 marginal ice zone. *Geophysical Research Letters*, 48, e2020GL090735, doi:10.1029/2020GL090735, 2021.
- Torres, T. S., Klein, P., Menemenlis, D., Qiu, B., Su, Z., Wang, J., Chen, S. and Fu, L.: Partitioning ocean motions into balanced motions and internal gravity waves: A modeling study in anticipation of future space missions. *J. Geophys. Res.-Oceans*, 123, 8084-8105, doi:10.1029/2018JC014438, 2018.
- Toyota, T., Kohout, A. and Fraser, A. D.: Formation processes of sea ice floe size distribution in the interior pack and its
410 relationship to the marginal ice zone off East Antarctica. *Deep-Sea Research Part II*, 131, 28-40, doi:10.1016/j.dsr2.2015.10.003, 2016.
- Uchiyama, Y., McWilliams, J. C. and Shchepetkin, A. F. Wave–current interaction in an oceanic circulation model with a vortex-force formalism: Application to the surf zone. *Ocean Modelling*, 34, 16-35, doi:10.1016/j.ocemod.2010.04.002, 2010.



- Wadhams, P. and Holt, B. Waves in frazil and pancake ice and their detection in Seasat synthetic aperture radar imagery. *J. Geophys. Res.-Oceans*, 96, 8835-8852, doi:10.1029/91JC00457, 1991.
- 415 Zhang, X., Dai, H., Zhao, J. and Yin, H.: Generation mechanism of an observed submesoscale eddy in the Chukchi Sea. *Deep Sea Research Part I*, 148, 80-87, doi:10.1016/j.dsr.2019.04.015, 2019.
- Zhang, X., Dai, H., Zhao, J. and Yin H.: Sensitivity study of the wave-driven current in an Arctic frazil-pancake ice zone. *Acta Oceanologica Sinica*, 3, 123-129, doi:10.1007/s13131-020-1560-x, 2020.
- 420 Zhang, Z., Tian, J., Qiu, B., Zhao, W., Chang, P., Wu, D. and Wan, X.: Observed 3D structure, generation, and dissipation of oceanic mesoscale eddies in the South China Sea. *Sci. Rep.*, 6, 24349, doi:10.1038/srep24349, 2016.
- Zhao, M., Timmermans, M.-L., Cole, S., Krishfield, R., Proshutinsky, A. and Toole, J.: Characterizing the eddy field in the Arctic Ocean halocline. *J. Geophys. Res. Oceans*, 119, 8800–8817, doi:10.1002/2014JC010488, 2014.